IOP Publishing | International Atomic Energy Agency Nuclear Fusion
Nucl. Fusion 57 (2017) 126048 (15pp) https://doi.org/10.1088/1741-4326/aa897e

Electromagnetic characteristics of geodesic acoustic mode in the COMPASS tokamak

J. Seidl[1], J. Krbec[1,2], M. Hron[1], J. Adamek[1], C. Hidalgo[3], T. Markovic[1,4], A.V. Melnikov[5,6], J. Stockel[1], V. Weinzettl[1], M. Aftanas[1], P. Bilkova[1], O. Bogar[1,7], P. Bohm[1], L.G. Eliseev[5], P. Hacek[1,4], J. Havlicek[1], J. Horacek[1], M. Imrisek[1,4], K. Kovarik[1,4], K. Mitosinkova[1,4], R. Panek[1], M. Tomes[1,4] and P. Vondracek[1,4]

[1] Institute of Plasma Physics, The Czech Academy of Sciences, Prague, Czech Republic
[2] Faculty of Nuclear Sciences and Physical Engineering, Czech Technical University in Prague, Prague, Czech Republic
[3] Laboratorio National de Fusión, CIEMAT, Madrid, Spain
[4] Faculty of Mathematics and Physics, Charles University, Prague, Czech Republic
[5] National Research Centre 'Kurchatov Institute', Moscow, Russian Federation
[6] National Research Nuclear University MEPhI, Moscow, Russian Federation
[7] Faculty of Mathematics, Physics and Informatics, Comenius University, Bratislava, Slovakia

E-mail: seidl@ipp.cas.cz

Received 17 January 2017, revised 14 August 2017
Accepted for publication 31 August 2017
Published 13 October 2017

Abstract

Axisymmetric geodesic acoustic mode (GAM) oscillations of the magnetic field, plasma potential and electron temperature have been identified on the COMPASS tokamak. This work brings an overview of their electromagnetic properties studied by multi-pin reciprocating probes and magnetic diagnostics. The $n = 0$ fluctuations form a continuous spectrum in limited plasmas but change to a single dominant peak in diverted configuration. At the edge of diverted plasmas the mode exhibits a non-local structure with a constant frequency over a radial extent of at least several centimeters. Nevertheless, the frequency still reacts on temporal changes of plasma temperature caused by an auxiliary NBI heating as well as those induced by periodic sawtooth crashes. Radial wavelength of the mode is found to be about 1–4 cm, with values larger for the plasma potential than for the electron temperature. The mode propagates radially outward and its radial structure induces oscillations of a poloidal $E \times B$ velocity, that can locally reach the level of the mean poloidal flow. Bicoherence analysis confirms a non-linear interaction of GAM with a broadband ambient turbulence. The mode exhibits strong axisymmetric magnetic oscillations that are studied both in the poloidal and radial components of the magnetic field. Their poloidal standing-wave structure was confirmed and described for the first time in diverted plasmas. In limited plasmas their amplitude scales with safety factor. Strong suppression of the magnetic GAM component, and possibly of GAM itself, is observed during co-current but not counter-current NBI.

Keywords: geodesic acoustic mode, tokamak, turbulence, COMPASS

(Some figures may appear in colour only in the online journal)

1. Introduction

Geodesic acoustic mode (GAM) [1] is a high-frequency oscillatory branch of zonal flows (ZFs) [2]. The zonal flows are turbulence-driven sheared poloidal flows which can play an important role in self-regulation of turbulent transport. By causing shear decorrelation of turbulent structures [3] ZFs contribute to establishing a saturated level of the turbulence and the energy transfer from turbulence to ZFs is believed to be an important part of the dynamics of the L-mode to H-mode (L-H) transition [4, 5] or I-mode [6].

As a kind of ZFs, GAM forms a toroidally symmetric ($n = 0$) oscillating poloidal flow with the plasma potential approximately constant on a flux surface ($m_\phi \approx 0$) and with a finite radial wave number k_r. Due to a geodesic curvature the flow couples to the $m_p = 1$ pressure perturbation with a standing wave pattern. Temperature oscillations associated with GAM have been reported as well [7]. The evidence of the finite radial wave number for GAM was reported e.g. in [8–10].

GAM oscillations are driven by a non-linear three-wave coupling with ambient turbulent oscillations [2], but can be destabilized also by an interaction with fast ions [11–13]. In practice, the non-linear coupling to turbulence is detected using bicoherence analysis [10, 14, 15]. Even though GAM is mainly an electrostatic mode, it can still generate a detectable perturbation of the magnetic field. The magnetic component has been recently described both in the theory [16–19] and experiment [7, 20–22]. While in circular plasmas the magnetic component has a standing wave structure with the poloidal mode number $m_B = 2$ [16, 20, 21], other Fourier components can be induced by plasma shaping [16] or due to mesoscale radial structure of the mode [20, 21].

Frequency of the mode in circular plasmas has been first derived in [1]. It scales with the ion sound speed c_s, the tokamak major radius R_0 and the safety factor q as

$$2\pi f_{\text{GAM}} = \left(2 + q^{-2}\right)^{1/2} c_s / R_0. \tag{1}$$

Here $c_s = \sqrt{(T_e + \gamma_i T_i)/m_i}$, T_e and T_i is the electron and ion temperature, respectively, m_i is the ion mass and γ_i is the ion specific heat ratio. However, experiments in the non-circular plasmas [23, 24] have shown GAM frequency lower than that predicted by the scaling (1), which led to the development of theoretical [16, 25, 26] and heuristic [23] scalings that incorporate also other geometrical factors, mainly the plasma boundary elongation κ_b. The frequency can change also due to the interaction with fast ions, in which case it often exhibits a chirping character [11, 12].

While the frequency smoothly changes over the plasma radius on some devices [10, 27], following the radial profile of c_s, other machines report one or more GAM non-local eigenmodes with the frequency forming radially localized plateaus of a constant value [8, 20, 23]. There are also reports of a global GAM eigenmode covering the whole plasma extent with a constant GAM frequency [28].

The non-local eigenmode structure of GAM can form when the GAM continuum has a maximum, e.g. due to reversed shear configuration [11] or presence of fast ions [29], but the radial structure of the mode can be influenced also by other factors such as β-coupling of poloidal harmonics [29]. GAM eigenmode radially propagating to the region with lower GAM frequency can also arise when finite gyroradius effects are taken into account [30]. Moreover, similarly to the $m_B = 2$ magnetic hallo, strong global $m = 2$ perturbation of the pressure, density and poloidal flow was derived for the continuum GAM in [16].

In this paper, we present observation of GAM oscillations in diverted deuterium discharges on the COMPASS tokamak. The mode is detected in a form of long range correlations of plasma potential between pair of reciprocating probes and in a form of axisymmetric oscillations of poloidal and radial magnetic field.

Several interesting properties of the mode are shown, such as: (i) poloidal structure of a magnetic hallo of the mode in diverted plasmas measured simultaneously in B_p and B_r components of the field, showing shift between the components in the poloidal angle, approximately by $\pi/2$ as predicted in [16], and distortion compared to an ideal $m_B = 2$ structure. (ii) Amplitude of the magnetic fluctuations in limited plasmas increases with safety factor, transition from a broad to a narrow spectrum of fluctuations is observed at high plasma shaping. (iii) Temperature oscillations at GAM frequency are detected, their radial propagation speed and radial wave number is different from that of the plasma potential. (iv) Injection of a co-current (but not counter-current) neutral beam suppresses the mode existing in ohmic plasma.

The article is organized as follows. In section 2 we begin with description of the used experimental setup. In section 3 we identify GAM oscillations in COMPASS plasmas and describe their properties. Namely, section 3.1 presents spectra of the measured signals, frequency of GAM and its temperature scaling are discussed in section 3.2, poloidal and radial structure of the mode is described in sections 3.3 and 3.4, respectively, and section 3.5 confirms the non-linear interaction between GAM and the ambient turbulence (AT). In section 4 we present initial observations of change of GAM amplitude in dependence on the direction of NBI. Finally, a brief summary is given in section 5.

2. Experimental setup

COMPASS ($R = 0.56$ m, $a = 0.2$ m) is a tokamak with an ITER-like plasma configuration, plasma current $I_p < 400$ kA, toroidal magnetic field $B_T < 2.1$ T and boundary elongation $\kappa_b \leqslant 1.85$ [31]. Auxiliary plasma heating is available using two NBI beams (40 keV) with a power of 350 kW each.

This study focuses mainly on diverted L-mode plasmas, where the presence of GAM has been confirmed in most of the available discharges and the mode is well accessible by both the probe and magnetic diagnostics. GAM presence has been confirmed also in limited discharges, but since in this case the mode is localized deeper in the plasma, further from the last closed flux surface (LCFS), the current database of deep probe plunges usable for the analysis of the mode is sparse and mainly magnetic data were used.

Figure 1(*a*) shows an example of a typical shape of plasmas analyzed in this work. All of the discharges had similar boundary elongation $\kappa_b \approx 1.8$ and the toroidal magnetic field $B_T = 1.15$ T. The lower and upper triangularity δ_l and δ_u, respectively, were linearly coupled to the elongation as $\delta_l \approx 0.56\kappa_b - 0.5$ and $\delta_u \approx 0.35\kappa_b - 0.3$. Unless noted otherwise, purely ohmic heating was used.

2.1. Probe diagnostics

COMPASS is equipped with two pneumatic reciprocating probe manipulators that can be used to detect electrostatic fluctuations associated with GAM. The manipulators are located at the top of the vessel and at the low-field side (LFS) mid-plane (figure 1(*a*)), toroidally shifted by 22.5° (figure 1(*b*)).

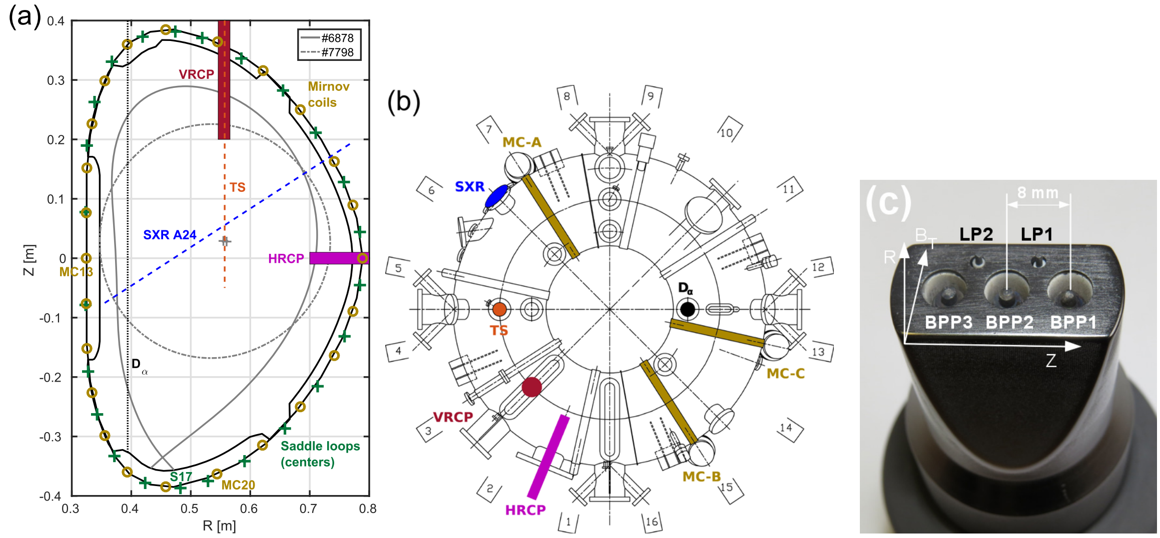

Figure 1. (*a*) Poloidal cross-section of the COMPASS tokamak showing layout of the used diagnostics together with a typical shape of the analyzed diverted and limited plasmas. (*b*) Top view of the tokamak with toroidal positions of the diagnostics. (*c*) Layout of probes on the horizontal probe head.

In the analyzed plasmas the manipulators were not directly connected by magnetic field lines. Schematic picture of the standard probe head used on the horizontal reciprocating manipulator (HRCP) is plotted in figure 1(*c*). It consists of several ball-pen probes (BPP) and Langmuir probes (LP) that are used to measure the floating potential of the BPP V_{BPP}, the floating potential of the LP V_{fl} and the ion saturation current I_{sat}, all with 5 MHz sampling rate. The potentials are measured on both manipulators but the I_{sat} only at the midplane. Since V_{BPP} is influenced by the electron temperature T_{e} much less than V_{fl}, as $V_{\mathrm{BPP}} \approx \phi - 0.7T_{\mathrm{e}}$ [32, 33], we use it as a close proxy to the real plasma potential.

The available combination of LPs and BPPs allows also estimation of local electron temperature T_{e} and its fluctuations using the formula [33]:

$$T_{\mathrm{e}} = \left(V_{\mathrm{BPP}} - V_{\mathrm{fl}}\right)/2.2. \quad (2)$$

In practice, the T_{e} measurement is limited by an incident heat flux on the Langmuir pin that can, in deeper parts of the plasma, cause LP self-emission [34]. In such a case the T_{e} measurement is lost but the self-emitting LP can be used as a cross-verification of the potential measurement by the BPP as $V_{\mathrm{BPP}} \approx V_{\mathrm{fl,self\text{-}emit}} \approx \phi - 0.7T_{\mathrm{e}}$ [33, 35].

Since BPP and LP are shifted poloidally by 4 mm, there is a risk that the temperature fluctuations could be dominated by an artificial phase-shift arising due to the non-locality of the measurement. Therefore, the temperature is evaluated from an average potential (BPP1 + BPP2)/2 that represents potential of a virtual BPP that is located at the poloidal position of the LP. This mitigates part of the phase-shift caused by the low-k_{p} part of the poloidal wave number spectra. The high-k_{p} does not seem to significantly contribute to the T_{e} fluctuations at the GAM frequency because of the strong poloidal flow of several km s^{-1}, which can advect small-scale structures between the probes on a time scale of several μs. This time scale is much shorter than the GAM period and such fluctuations, possibly affected by the artificial phase shift, are thus filtered out when the T_{e} signal is band-pass filtered around the GAM frequency.

Both manipulators are able to reciprocate inside the last closed flux surface without overheating of the probe head. However, the position of the probes is not in a full agreement with the LCFS determined by an EFIT reconstruction. A typical shift at the LFS midplane is less than 1 cm in the circular plasmas but of about 2 cm in the diverted ones. As both probes can provide measurement of the local T_{e}, we therefore carry out magnetic surface labeling, that is necessary for a comparison of the data at the two poloidal positions, using an assumption that T_{e} is constant over flux surface. This is justified by a short distance along field line between both poloidal positions, which is comparable or smaller than the electron mean free path in the edge, allowing for a fast energy exchange between the two positions. It is also supported by a reasonable match between the temperature profiles when an EFIT correction is applied [33]. Nevertheless, an influence of possible poloidal asymmetries in the plasma edge on the surface labeling using T_{e} cannot be fully excluded.

Since a direct measurement of the plasma potential is available, we use it for radial localization of the measurements with respect to the radius of a zero radial electric field $R_{E_{\mathrm{r}}=0}$. At the LFS midplane the radius is defined as a position where $E_{\mathrm{r}} = -\partial\langle\phi\rangle/\partial r \approx -\partial\langle\phi\rangle/\partial R = 0$ and a similar definition is used for the vertical position $Z_{E_{\mathrm{r}}=0}$. This reference point, that marks location of the edge sheared poloidal flows, can be directly measured by the probes in any ohmic or L-mode discharge with a sufficiently deep probe plunge. Here, $\langle\cdot\rangle$ represents a radial profile computed either by bin-averaging or by low-pass filtering of the original 5 MHz data by higher-order Butterworth filter with 200 Hz cut-off frequency. Such cut-off frequency is high enough not to distort the profiles due to the radial movement of the probe with velocity $v_{\mathrm{rcp}} \approx 0.5$–$1$ m·s^{-1} and at the same time low enough to remove an influence of sawtooth oscillations that in ohmic

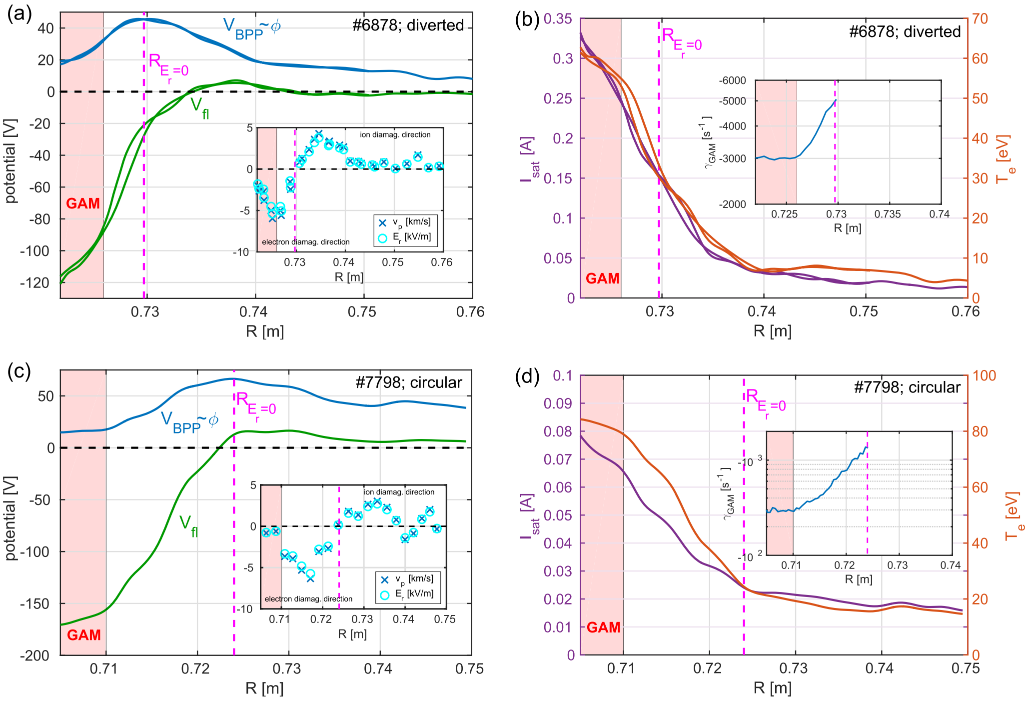

Figure 2. Radial profile of the mean plasma potential ϕ and floating potential V_{fl}, in diverted (*a*) and limited circular (*c*) plasmas. Radial profile of the mean ion saturation current I_{sat} and electron temperature T_{e} in diverted (*b*) and limited (*d*) plasmas. Measured by HRCP at the LFS midplane. The inset plots in (*a*) and (*c*) show radial profile of the radial electric field E_{r} and radial profile of the mean poloidal $E \times B$ velocity $\langle v_{\mathrm{p}} \rangle$. The inset plots in (*b*) and (*d*) show radial profile of a combined Landau and collisional damping evaluated from the data. Dashed magenta line marks position $R_{E_{\mathrm{r}}=0}$. Data from #6878 are plotted for both directions of probe movement (inward and outward). Pink area marks radial location of GAM oscillations visible in the potential power spectra.

discharges appear at frequencies above 300 Hz and may temporarily change edge plasma parameters.

Typical radial profiles of $\langle \phi \rangle$, $\langle V_{\mathrm{fl}} \rangle$ and $\langle E_{\mathrm{r}} \rangle$ measured by the HRCP in the SOL of diverted and circular plasmas are shown in figure 2. One can readily see a significant difference between the plasma potential approximated by V_{BPP} and the floating potential of a Langmuir probe V_{fl}. The difference is proportional to the local electron temperature (equation (2), figures 2(*b*) and (*d*)). Local maximum of V_{BPP} defines the reference radius $R_{E_{\mathrm{r}}=0}$ with $E_{\mathrm{r}} = 0$ and thus the place of reversal of the direction of a poloidal $E \times B$ flow $\langle v_{\mathrm{p}} \rangle = -\left(\partial \langle \phi \rangle / \partial r\right) / B$. In the analyzed discharges the maximum magnitude of the mean poloidal flow typically reached 5–6 km s^{-1}, with the maximum located inside $R_{E_{\mathrm{r}}=0}$. The absolute value of poloidal shearing rate $\omega_{E \times B} = \partial \langle v_{\mathrm{p}} \rangle / \partial r$ on the other hand peaked typically at or very close to the position $R_{E_{\mathrm{r}}=0}$.

Since V_{fl} drops at the position of the GAM mode to very low values ($V_{\mathrm{fl}} < -100$ V), biasing voltage of the LP used for I_{sat} measurement was adjusted appropriately to $V_{\mathrm{bias}} = -270\ \mathrm{V} \ll V_{\mathrm{fl}}$.

Figures 2(*b*) and (*d*) show that the radial I_{sat} and T_{e} profiles are steepened around the position of $R_{E_{\mathrm{r}}=0}$ radius, and they flatten in the SOL. This is consistent with the definition of near and far SOL [36]. Another flattening of the temperature profiles is observed in the plasma, inside the $E_{\mathrm{r}} = 0$ radius. This indicates that the profile steepening may be linked to the presence of the velocity shear layer around $R_{E_{\mathrm{r}}=0}$ and possibly also to the presence of the LCFS in this region. Even though the hypothesis $R_{E_{\mathrm{r}}=0} \approx R_{\mathrm{LCFS}}$ could not be directly verified on COMPASS, similar BPP measurements on ASDEX Upgrade show good correspondence of both locations [37] and good agreement has been found also in stellarators [38]. Therefore, since the position of $R_{E_{\mathrm{r}}=0}$ is measured simultaneously with the analyzed data by the same diagnostics, it is used as a reliable reference point and as a proxy for the position of the LCFS. The question of a precise localization of the LCFS with respect to the velocity shear layer in COMPASS plasmas is left open for a further study.

2.2. Magnetic diagnostics

COMPASS is equipped with three poloidal rings of magnetic Mirnov coils (MC) labeled MC-A, MC-B and MC-C, each capable of measuring all three components of the magnetic field. Their poloidal coverage is shown in figure 1(*a*) and toroidal positioning in figure 1(*b*). In order to detect magnetic fluctuations associated with GAM, the probe diagnostics was supplemented by measurement of fluctuations of poloidal (tangential to the first wall) and radial (normal to the first wall) components of magnetic field B_{p} and B_{r}, respectively, with 2 MHz sampling rate along the full poloidal cross-section.

Moreover, a set of saddle loops, that are divided into four toroidal quadrants and poloidally cover most of the vessel (see figure 1(*a*) and [39]), was used for measurement of axisymmetric $n = 0$ part of B_{r} fluctuations at 24 poloidal positions.

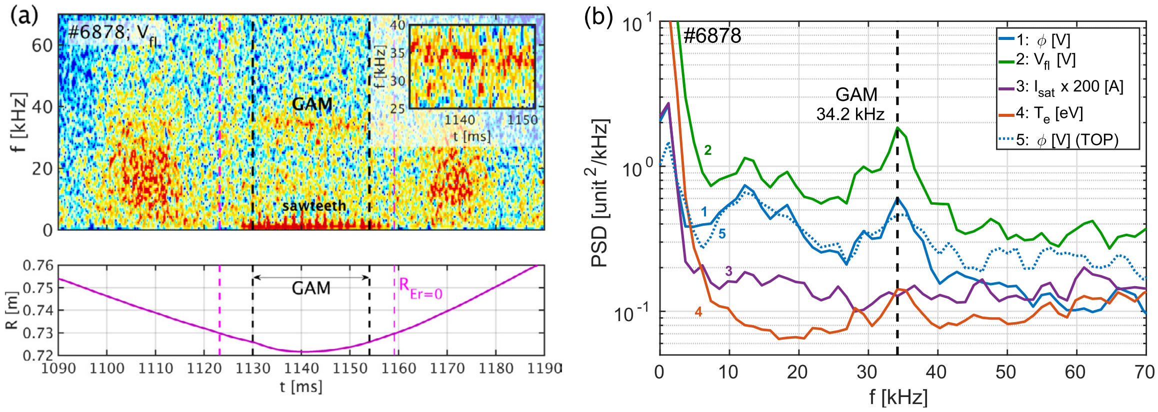

Figure 3. (*a*) Spectrogram of V_{fl} during reciprocation of HRCP. Probe position in time is shown at the bottom. Magenta lines mark position of the $R_{E_r=0}$ radius and black vertical lines mark the appearance of GAM. The radial localization of the GAM region corresponds to that marked in figures 2(*a*) and (*b*) by the pink background. The inset plot zooms the spectrogram on the GAM oscillations. (*b*) Power spectral density of HRCP (solid) and VRCP (dotted) signals in the discharge #6878, 8 mm inside $R_{E_r=0}$ at HRCP and 5 mm inside $Z_{E_r=0}$ at the top.

2.3. Other diagnostics

Line averaged density n_e is measured by a single-channel interferometer ($\lambda = 2$ mm) along a central vertical chord. High-resolution Thomson scattering system (TS) [40, 41] is used to obtain electron temperature and density profiles vertically at the top of the plasma with spatial resolution ~3–4 mm and temporal resolution 16 ms. The relatively low temporal resolution is increased by combining TS data with fast measurement of relative temperature changes by an ECE/EBW system [42]. Neutral particle analyzer (NPA) provides ion temperature in the center of the plasma. To approximate profiles of T_i with respect to the normalized poloidal flux ψ_N we use formula $T_i(\psi_N) = \{T_i(\psi_N = 0) + [T_e(\psi_N = 0) - T_i(\psi_N = 0)]\psi_N\}[T_e(\psi_N)/T_e(\psi_N = 0)]$. Single central chord (figure 1(*a*)) of a multi-chord SXR system is used to monitor soft-x-ray (SXR) radiation in the plasma center and to detect temporal evolution of a sawtooth instability in the plasma center.

3. GAM oscillations

On COMPASS, an electrostatic as well as magnetic component of GAM oscillations can be observed. First, we describe localization of the mode on the data from the horizontal reciprocating probe. Figure 3(*a*) shows spectrogram of the V_{fl} signal during movement of HRCP in the flat-top of a diverted discharge (#6878, $I_p = 170$ kA, $n_e = 3.5 \times 10^{19}$ m^{-3}, $q_{95} = 4.6$). As soon as the probe gets several millimeters inside the $R_{E_r=0}$ radius, it starts to register intermittent GAM oscillations at frequency f_{GAM} ~ 35 kHz. The situation is similar also in circular discharges but the observed GAM frequency is higher (>40 kHz) and the GAM mode is detected significantly deeper in the plasma (compare the pink areas in the figures 2(*a*) and (*c*)). GAM extends from this point radially into the plasma throughout the whole range that the probe can penetrate before becoming overheated (typically 1–2 cm from $R_{E_r=0}$ at the LFS but even more than 3 cm at the top) and probably continues further inward.

Appearance of GAM is a combined effect of its drive and damping. As the combination of a collisional and Landau damping [43] in the edge is approximately 5–10 times higher in the diverted case (compare insets of figures 2(*b*) and (*d*)), where the mode is detected closer to the edge, the observed difference in the GAM localization is not caused by a difference in the absolute value of GAM damping rate. Nevertheless, GAM edge correlates with the radius where T_e profile suddenly steepens towards SOL, which will cause faster GAM suppression due to a relative increase of the collisional damping compared to the plateau present in the GAM region. Moreover, an inward radial shift in the edge turbulence characteristics, which may influence also drive of the mode, comparable to the shift of GAM edge, was found in plasmas with low elongation. Localization of a transition region between the hole-dominated (inside, negative skewness of density fluctuations) and blob-dominated (outside, positive skewness) regions, where number of blobs and holes is balanced and PDF of density fluctuations is Gaussian, roughly corresponds in both cases to the GAM edge.

3.1. Spectra of electrostatic and magnetic components

Since poloidal structure of GAM is $m_\phi \approx 0$ in the potential and $m_n \approx 1$ in the density (with the node of oscillations localized at the midplane) and also $\delta n/n = \sqrt{2}k_r\rho_i\delta\phi/(eT_e)\sin(\theta) \gg \delta\phi/(eT_e)$ [2], where θ is the poloidal angle, k_r is the GAM radial wavenumber, ρ_i is the ion Larmor radius, and $k_r\rho_i < 1$, it is expected that close to the midplane GAM should exhibit significant oscillations of ϕ but no or only weak oscillations of I_{sat} or density (as shown e.g. in [44]). This is confirmed by a power spectral density (PSD) of probe signals plotted in figure 3(*b*). The PSD was computed over the whole region where the GAM oscillations are present in the probe signals (see black dashed lines in figure 3(*a*)) and it shows a clear peak on ϕ and V_{fl}, i.e. oscillations linked to the plasma potential, both at the LFS and the top, but no peak in the spectra is present on the I_{sat} signal at the LFS, which is consistent with the basic model of the GAM poloidal structure. Absence of the I_{sat} fluctuations is further confirmed by a negligible cross-coherence between the I_{sat} and both potential signals, that was evaluated at the GAM frequency. Interestingly, the

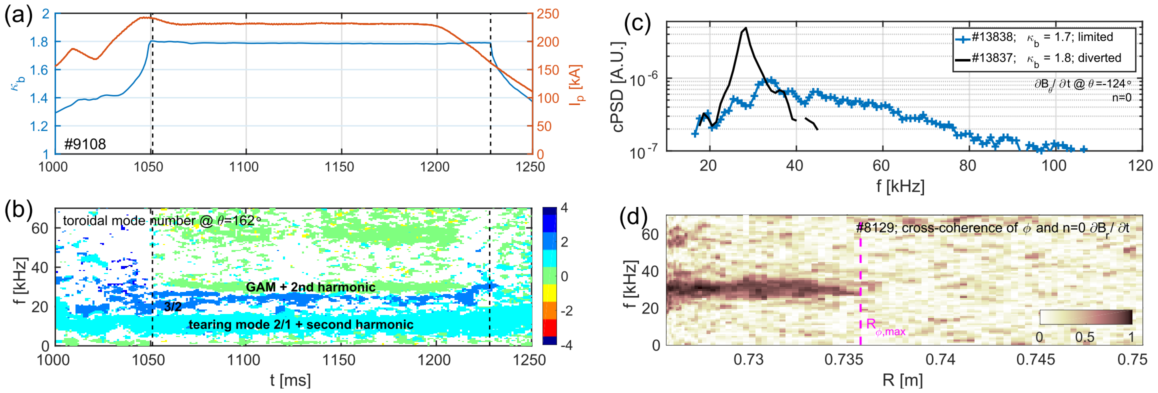

Figure 4. (*a*) Plasma current and boundary elongation in the discharge #9108. (*b*) Toroidal mode number of $\partial B_p/\partial t$ oscillations in #9108 evaluated from the cross-phase of toroidally shifted Mirnov coils MC-C13 and MC-B13. Vertical lines mark diverted phase of the discharge. (*c*) Coherent part of the $n = 0$ $\partial B_p/\partial t$ spectra in the case of a diverted and a strongly elongated discharge. (*d*) Cross-coherence of the $n = 0$ component of $\partial B_r/\partial t$ signal and fluctuations of the plasma potential at midplane.

oscillations in ϕ and V_{fl} are not identical, which implies presence of a small oscillation in T_e in the order of $\delta T_e \approx 1$–2 eV or $\delta T_e/T_e \sim 2\%$ (for more details see figure 13(*d*) in section 3.4).

GAM is not a purely electrostatic mode and it is expected to exhibit also electromagnetic features. In COMPASS diverted discharges the magnetic GAM component is strong enough to be directly measured by Mirnov coils and saddle loops. This is demonstrated in figures 4(*a*) and (*b*) that show time evolution of modes visible in the spectra of $\partial B_p/\partial t$ signals at the HFS midplane in discharge #9108 ($I_p = 230$ kA, $n_e = 6.5 \times 10^{19}$ m^{-3}, $q_{95} = 3.5$). While there is no clear $n = 0$ mode (green color) visible in the limited phase of the discharge, at about the same time when the X-point is created, axisymmetric oscillations attributed to GAM appear at frequency 29 kHz. The oscillations last until the end of the flat top phase and disappear when the elongation is decreased and the plasma becomes limited again. To confirm that the magnetic oscillations are related to the oscillations of the plasma potential, a cross-coherence of both has been computed and plotted in figure 4(*d*).

In the limited plasmas, the magnetic GAM oscillations are still present, both in B_p and B_r, but with a weaker amplitude, often below the background level, and somewhat different poloidal structure, visible only at HFS around $\theta \approx \pm(90$–$135)°$.

Figure 4(*c*) shows difference in coherent spectra of $\partial B_p/\partial t$ for a strongly shaped limited plasma and the diverted plasma. The coherent spectrum cPSD was computed to limit the effect of the background fluctuations as $\mathrm{cPSD}(f) = c_{AC}(f)\mathrm{PSD}_A(f)$, where $c_{AC}(f)$ is the cross-coherence between two toroidally separated poloidal Mirnov coils from rings *A* and *C* and PSD_A is the power spectral density of the coil *A*. Data points at frequencies with non-zero cross-phase, i.e. $n \neq 0$, were removed. While only a single peak is present in diverted cases ($\kappa_b \geqslant 1.8$, $\delta_l \geqslant 0.5$), the spectrum is significantly broader in the limited plasmas ($\kappa_b \leqslant 1.75$, $\delta_l \leqslant 0.46$), with detectable $n = 0$ oscillations and non-negligible cross-coherence in the range 25–100 kHz. This suggests that in the latter case the coils pick up GAM oscillations coming from different plasma regions with different f_{GAM}, likely from a continuum GAM. With shaping increased close to $\kappa_b \approx 1.7$ a small peak typically

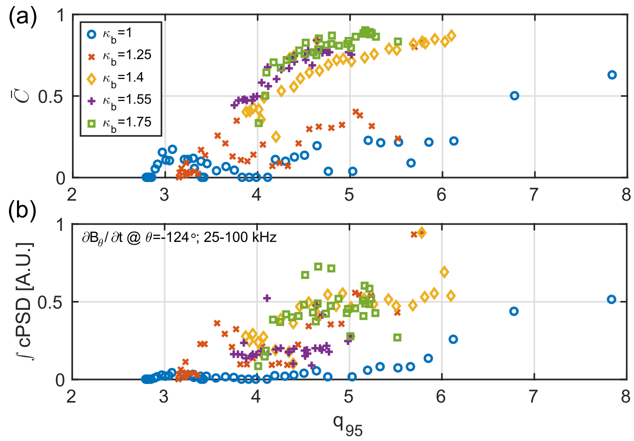

Figure 5. Dependence of the mean cross-coherence between Mirnov coils MC-A17 and MC-C17 (*a*) and integral of the coherent part of the spectra cPSD (*b*) in the frequency range 25–100 kHz on edge safety factor and elongation in a series of current ramp-up discharges ($n_e = 3$). Frequencies with a non-zero phase shift were set to 0 during the averaging/integration.

starts to form around 30 kHz at the bottom part of the broad spectra, i.e. in the plasma edge. When the shaping further increases above $\kappa_b \approx 1.75$ and an X-point is formed, a formation of a single dominant non-local GAM with strong magnetic oscillations around a single frequency is triggered, while the rest of the $n = 0$ spectra typically becomes suppressed. Properties of this dominant mode will be described in the rest of the paper.

As the Landau damping increases with q, the GAM amplitude is expected to scale with q as well. Similar trend is observed for the magnetic component of the broadband GAM oscillations in the limited plasmas. Figure 5(*a*) shows mean coherence between two toroidally shifted Mirnov coils in the GAM frequency range 25–100 kHz, where contributions of $n \neq 0$ parts of the spectra were set to zero, plotted as a function of q_{95} and boundary elongation κ_b. This represents a relative amplitude of the GAM activity in this frequency range with respect to the background fluctuations. The relative amplitude clearly increases with q_{95} and also with the plasma shaping. The increase with q_{95} is visible also for the absolute

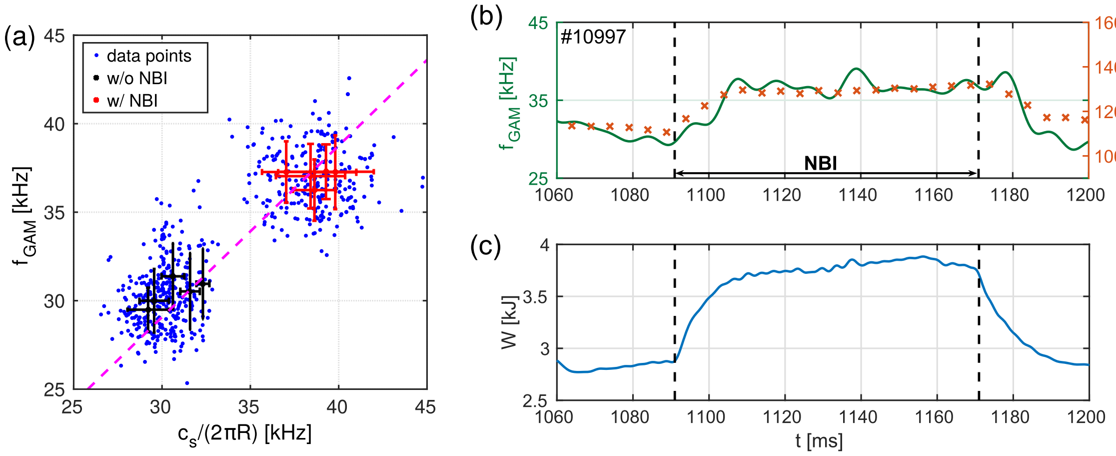

Figure 6. (*a*) GAM frequency versus ion sound speed at radial position $\psi_N = 0.85$ in ohmic (1066–1090 ms; black crosses) and CO-NBI (1139–1161 ms; red crosses) phases of NBI heated discharges. The magenta dashed line represents $y = 0.98x$. The blue dots represent the same data but sampled every 0.1 ms. (*b*) Temporal evolution of the GAM frequency during one discharge compared with the edge ion sound speed. (*c*) Temporal evolution of the plasma energy from EFIT.

amplitude, represented by an integral of the coherent spectrum cPSD in the same frequency range (figure 5(*b*)).

3.2. Scaling of GAM frequency with the ion sound speed

A typical range of GAM frequencies f_{GAM} observed on COMPASS in diverted ohmic deuterium plasmas is 25–40 kHz. According to the local model (1), f_{GAM} should scale with a square root of the plasma temperature. A series of discharges with co-current NBI (CO-NBI) heating was performed to test the temperature dependence of frequency of the studied mode. We note that the NBI did not alter most of the plasma parameters in the edge, including plasma shape, profile of q or density. The NBI affected mainly plasma temperature and possibly also plasma rotation, which is, however, not measured.

The GAM frequency was extracted using Hilbert transform from Mirnov coil signal MC-A20 band-pass filtered around the GAM peak in the power spectra. The Hilbert transform provides temporal evolution of an instantaneous frequency of the oscillation and low-pass filter at 1 kHz was further applied to reduce the noise but to still keep the evolution of the frequency on a time scale of the sawtooth period. Blue points in figure 6 represent values of f_{GAM} and c_s down-sampled to 0.1 ms resolution. In order to identify radial position whose temperature governs the frequency of the mode, assuming that it does not change when the NBI is applied, we performed a linear regression of the measured frequency before and during NBI heating versus local c_s at several radii in the range $\psi = 0.6$–0.99. The case with the lowest misfit given by the weighted total least squares estimate [45] was found at $\psi = 0.85$ and is plotted in figure 6(*a*) showing a linear scaling of f_{GAM} with the edge ion sound speed.

Data points used in the regression and shown in figure 6(*a*) represent f_{GAM} and c_s in the ohmic phase of the discharge (black) and after reaching an NBI-heated equilibrium (red). Time evolution of the frequency, edge c_s, and plasma energy during one discharge, including a transition period, is shown in more detail in figures 6(*b*) and (*c*). Here the GAM frequency changes smoothly and in relation to the change of plasma energy caused by the NBI, following evolution of local c_s.

Due to a presence of the sawtooth instability, the temperature of the plasma has often a non-negligible temporal evolution even in the flat-top phase of the discharge. After each sawtooth crash, an energy is expelled from the core and propagates towards the plasma boundary on a timescale of several hundreds of microseconds, where it can temporarily change the local temperature by tens of percent [31] as is demonstrated in figure 7(*a*) (#8848, $I_p = 210$ kA, $n_e = 2.5 \times 10^{19}$ m^{-3}, $q_{95} = 3.7$). Comparison of edge and core diagnostics shows that a typical delay between the sawtooth crash in the center and the perturbation of the edge is approx. 100–500 μs.

Since GAM frequency is temperature dependent, one would expect periodic oscillations of f_{GAM} with the sawtooth period, similar to the behavior reported on T-10 [22]. While the GAM signal on the electrostatic probes is intermittent (see zoom of the V_{fl} spectrogram in figure 3(*a*)) and larger statistics than that currently available would be needed to follow the temporal evolution of the frequency, the temporal oscillations of f_{GAM} can be visualized on magnetic diagnostics during a strong sawtooth activity.

Figures 8(*a*) and (*b*) show a wavelet spectrogram of a $\partial B_p/\partial t$ signal compared with the central SXR channel. A conditionally averaged evolution of the spectrogram during the sawtooth period is plotted in figure 8(*c*). The conditional average was performed over 100 ms of the flat-top (#11506, $I_p = 200$ kA, $n_e = 4.5 \times 10^{19}$ m^{-3}, $q_{95} = 3.7$), the drops of the central SXR that indicate a time of the sawtooth crash in the center were used as triggers. Each drop of the SXR signal (figure 8(*e*)), caused by an expulsion of energy from the core, is followed by an increase of f_{GAM} delayed by approx. 300 μs, i.e. the time is comparable to the time needed for the energy to propagate from the core to the plasma edge. However, it still comes before the pulse arrives into the SOL as indicated by the delay of a peak in D_α emission in figure 8(*d*). After the initial sharp increase, the frequency gradually relaxes back to its initial value in a way that is similar to the behavior of T_e in

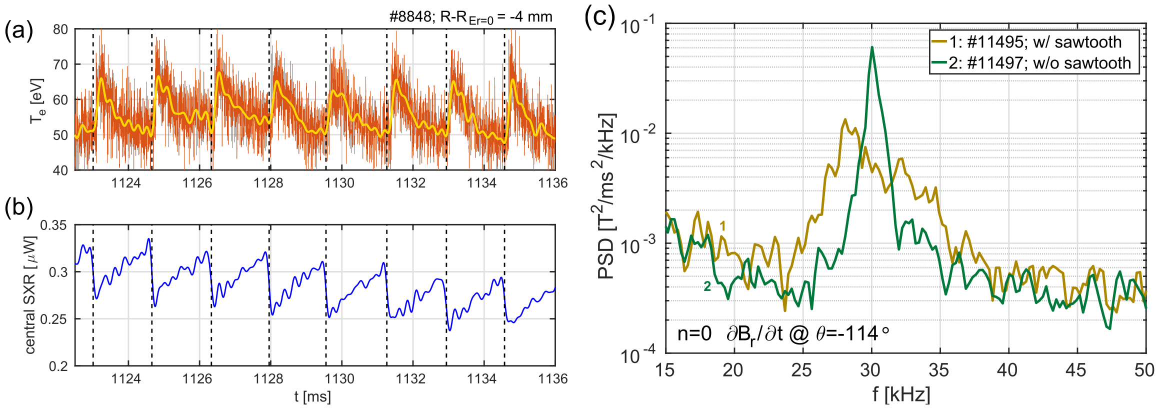

Figure 7. Evolution of the edge plasma temperature measured by HRCP (*a*) and the core emission of SXR (*b*). (*c*) PSD of an axisymmetric part of $\partial B_r/\partial t$ fluctuations in the divertor region in two similar discharges with (gold, 1) and without (green, 2) sawtooth instability.

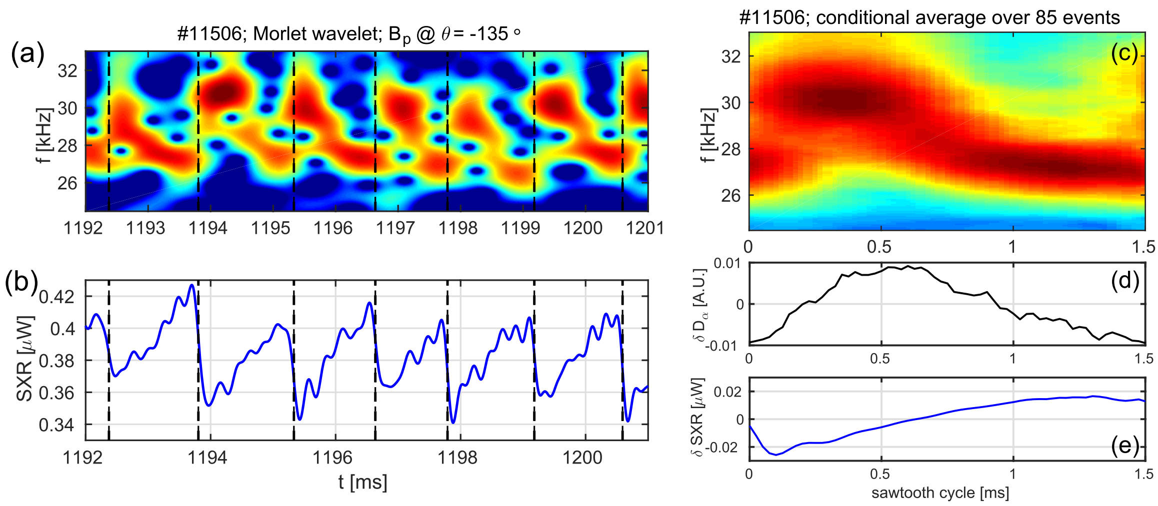

Figure 8. Wavelet spectrogram of $\partial B_p/\partial t$ at MC-A20 during a strong sawtooth activity (*a*) and the core emission of SXR (*b*). Conditional average of (*a*) and (*b*) and perturbation of D_α emission over 85 sawtooth crashes is shown in (*c*)–(*e*).

figure 7(*a*). The observed change of the frequency would, due to the f_{GAM} dependence on c_s, correspond to a relative change of plasma temperature in the order of tens of percent, i.e. well within the observed range. At this moment, however, the outlined relation between oscillations of f_{GAM} and edge T_e cannot be proved quantitatively since a fast measurement of edge T_e was not available due to overheating of the Langmuir pin by the large sawteeth in the same discharges where significant oscillations of f_{GAM} were measured by the magnetic coils.

The temporal oscillations of f_{GAM} then explain the relative width of the GAM PSD in figures 3 and 4. Figure 7(*c*) shows difference of the PSD in an ohmic phase of two similar discharges (I_p = 180 kA, $n = 4.5 \times 10^{19}$ m^{-3}, $q_{95} = 3.6$) following 80 ms of CO-NBI heating. In one of them (P_{NBI2} = 270 kW) the NBI power was sufficient to stabilize the sawtooth instability leading to a narrow GAM peak $\delta f_{GAM}/f_{GAM} \sim 0.13$ while in the other one (P_{NBI2} = 220 kW) the sawtooth instability is present and the GAM peak remains broad, $\delta f/f \sim 0.38$. As visible from figure 8, the broad double-peaked structure of PSD observed in discharges with sawteeth (yellow line in figure 7) does not correspond to a simultaneous presence of two or more modes co-existing at close frequencies, but rather to a temporal evolution of a single mode. When the perturbation caused by sawteeth is not present, the peak remains narrow. Absence of the sawteeth also increased the GAM amplitude, represented either by the area under the GAM peak in PSD or by a variance of fluctuations in the range 24–36 kHz, both by 35%.

Even though f_{GAM} changes with heating power and it seems to react also on temporal evolution of plasma temperature during the sawtooth cycle, the frequency remains constant in space and does not scale with radial profile of local electron temperature in the edge layer penetrated by the probes. Figure 9 compares f_{GAM} estimated from the spectra of a plasma potential measured by VRCP at the top of a hydrogen plasma (#11162, I_p = 200 kA, $n_e = 8 \times 10^{19}$ m^{-3}, $q_{95} = 3.9$) with a local profile of $\sqrt{T_e}$ measured by the same probe head. In the case of a local GAM the frequency scaling given by the equation (1) holds locally and the profile of f_{GAM} should follow the profile of $\sqrt{T_e}$, assuming a constant ratio of T_i/T_e at the edge and neglecting a change of q. However, as figure 9 shows, in COMPASS plasmas the frequency remains approximately constant while $\sqrt{T_e}$ changes by a factor of 1.5. This indicates presence of a non-local GAM with a frequency plateau in the radial direction. The extent of the plotted data is limited by the range of probe measurements but the frequency plateau seems

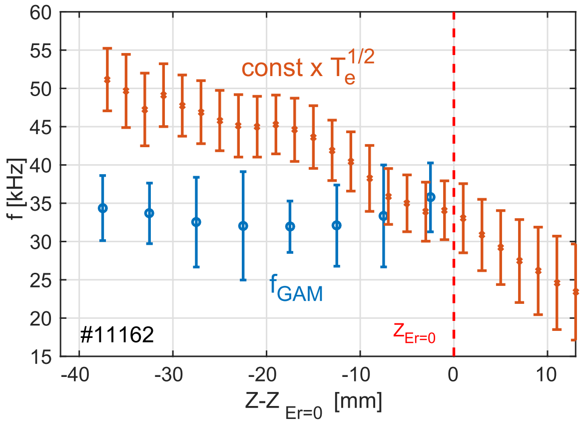

Figure 9. Spatial profile of f_{GAM} (blue) and of $\sqrt{T_{\mathrm{e}}}$ scaled to fit f_{GAM} around $Z_{E_{\mathrm{r}}=0}$ (orange).

to continue further inward. Currently it is not clear what is the full radial extent of the GAM and at which radius does the mode originate. Two examples from other devices show that a non-local mode can form radially localized plateau regions as on AUG [23] or it could even span the whole plasma as on T-10 [28].

3.3. Poloidal structure

While axisymmetric in all fields, GAM is expected to have different poloidal mode numbers in plasma potential, m_ϕ, density, m_n, and magnetic field, m_B.

The oscillations of plasma potential should be constant on a flux surface with mode numbers $m_\phi/n \approx 0/0$. This structure implies presence of long-range correlations (LRC) with a zero phase shift at the GAM frequency between plasma potential measured at two poloidally and toroidally displaced parts of a single flux surface. On COMPASS, this can be detected using the pair of reciprocating probes that are located at the LFS and top of the plasma and toroidally shifted. This is shown in figure 10 using cross-coherence of V_{fl} during a simultaneous deep plunge of the probes (#7732, $I_{\mathrm{p}} = 200$ kA, $n_{\mathrm{e}} = 4 \times 10^{19}$ m^{-3}, $q_{95} = 4$). An increased value of the coherence clearly appears shortly after both probes enter the relevant area inside the $R_{E_{\mathrm{r}}=0}$ radius and disappears just before the first of them leaves it. On the same flux surface, marked by the black dashed vertical line, the cross-coherence of the signal reaches 0.9 and the mutual phase shift is close to zero (figure 10(*c*)), $\Delta\varphi = 0.1\pi$, consistent with $n/m_\phi \approx 0/0$ expected for GAM.

This observation is further supported by an estimation of a wavenumber-frequency spectra [46] from two-point measurements of two BPPs located on the horizontal manipulator and separated vertically by 1.6 cm. This method assumes that the measured signals consist of a superposition of wave packets characterized by the wave number $k(f)$ and frequency f. When two signals measured at the distance Δx are divided into M realizations of an equal length, the local wavenumber-frequency spectrum $S(k, f)$ can be estimated as

$$S(k,f) = \frac{1}{M}\sum_{j=1}^{M} I_{\Delta k}\left(k - k^j(f)\right) \times \frac{1}{2}\left[S_1^j(f) + S_2^j(f)\right]. \tag{3}$$

Here, S_1^j and S_2^j are power spectra of the signals, $k^j(f) = \Delta\varphi_{12}^j(f)$ is a local wave number, $\Delta\varphi_{12}^j(f)$ is a cross-phase between the signals in the realization j, and $I_{\Delta k}(x)$ is an indicator function such that $I_{\Delta k}(x) = 1$ for $x < \Delta k$, and 0 otherwise.

Based on the wavenumber-frequency spectrum $S(k, f)$ one can define also the statistical dispersion relation

$$\bar{k}(f) = \int kS(k,f)\,\mathrm{d}k \Big/ \int S(k,f)\,\mathrm{d}k \tag{4}$$

and the wavenumber spectrum width

$$\sigma_k(f) = \sqrt{\int \left(k - \bar{k}(f)\right)^2 S(k,f)\,\mathrm{d}k \Big/ \int S(k,f)\,\mathrm{d}k}. \tag{5}$$

$S(k, f)$ estimated from 285 ms of two-point ϕ measurements collected from several identical discharges (#9548-9559, $I_{\mathrm{p}} = 200$ kA, $n_{\mathrm{e}} = 3 \times 10^{19}$ m^{-3}, $q_{95} = 3.8$) and carried out by BPP1 and BPP3 in the GAM region is plotted in figure 10(*d*). The estimate of the GAM poloidal wavenumber and the wavenumber spectrum width computed using the equations (4) and (5) is $\bar{k}_{\mathrm{p}}(f_{\mathrm{GAM}}) = 0.01 \pm 0.08$ cm^{-1}, which corresponds to the poloidal mode number $m_\phi = 0.2 \pm 1.4$. The mean value is close to $m_\phi \approx 0$ within the precision given by a radial misalignment of the probe pins with respect to the magnetic surfaces, estimated from an EFIT reconstruction as ~0.1–0.2 cm, and the fact that $k_{\mathrm{r}} \gg k_{\mathrm{p}}$ (see section 3.4 for estimation of k_{r} in the same type of discharge).

In the case of the magnetic component, a standing wave with $m_B = 2$ structure shown in figure 11(*g*) is predicted for circular plasmas [16, 19] and has been previously confirmed on several devices [20, 21]. However, additional Fourier components can be excited as an effect of plasma shaping [16], radial width of the mode or plasma beta [17, 18]. Poloidal structure of the amplitude and phase of the GAM magnetic component in a diverted COMPASS plasma without sawteeth is plotted in figures 11(*a*)–(*f*) for two components of the magnetic field, B_{r} and B_{p}. The structure exhibits phase jumps by ~π, confirming the non-rotating standing wave structure of the oscillations, even though the poloidal structure is more complex than simple $m_B = 2$. The B_{r} field (figure 11(*c*)) has two regions of a constant phase shift $\varphi \sim \pi$ at the top and bottom of the plasma, consistent with GAM in an ideal circular plasma, but the bottom one is relatively narrow and an additional region with $\varphi \sim \pi$ and low amplitude of oscillations appears around HFS midplane. In the B_{p} field, the bottom HFS part seems to have a mixed phase of $\varphi \sim \pi/2$ and an additional region with $\varphi \sim \pi$ appears at the bottom LFS.

The amplitude of the magnetic oscillations plotted in figure 11 has been estimated in a 5 kHz frequency band centered around f_{GAM}. The oscillations in B_{r} are about one order of magnitude weaker than in B_{p}. GAM is strongest in both

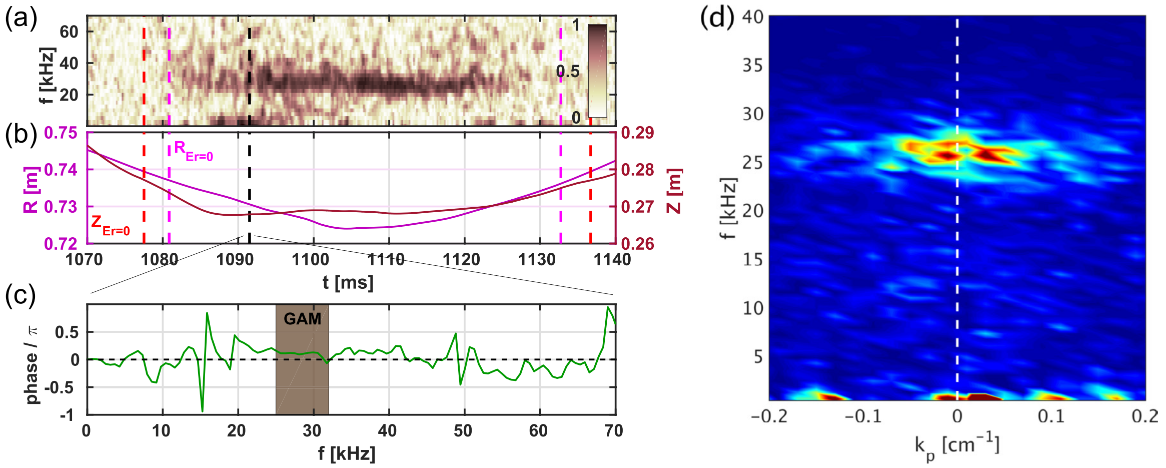

Figure 10. (*a*) Cross-coherence of V_{fl} at the top and LFS midplane measured by HRCP and VRCP in discharge #7732. (*b*) Position of the probes in time. The vertical black dashed line marks the time when both probes are at the same flux surface; red and magenta dashed lines mark crossing of the position of $E_{\mathrm{r}} = 0$. (*c*) Cross-phase of the V_{fl} oscillations measured simultaneously on the same flux surface at the top and LFS midplane. The brown region marks the GAM frequency. (*d*) Poloidal wavenumber-frequency spectrum of plasma potential fluctuations measured by HRCP at the outer midplane using two BPPs separated vertically by 1.6 cm.

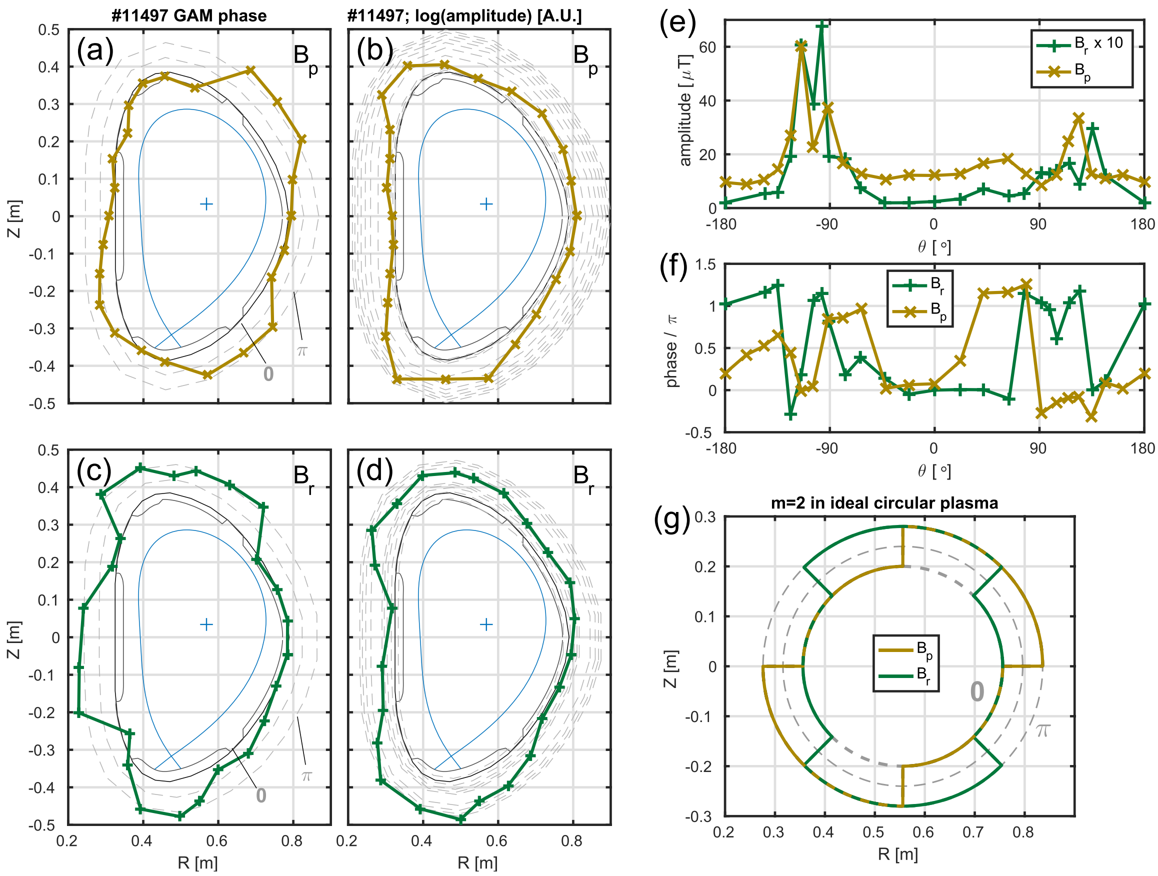

Figure 11. Poloidal structure of the GAM phase shift (*a*), (*c*) and (*f*) and structure of the standard deviation of magnetic fluctuations around the GAM frequency (*b*), (*d*) and (*e*) for the $n = 0$ component of B_{r} field (*c*)–(*f*) and the local B_{p} field (*a*), (*b*), (*e*) and (*f*). GAM phase with the $m = 2$ structure predicted for an ideal circular plasma is shown in (*g*). Contours of a constant value are marked in (*a*)–(*d*) by the gray dashed lines and follow rescaled shape of the vessel.

components at the bottom and the top of the plasma, somewhat shifted to the HFS, and weak on midplane. This is similar to the GAM structure observed on TCV [20]. The regions of the non-standard phase shift exhibit an overall low amplitude of oscillations and can thus be considered to be only a minor perturbation of the GAM structure.

3.4. Radial structure

In order to determine radial structure of GAM, two methods were used. First, we have used the $n = 0$ component of saddle loops S17 as a reference signal and computed cross-phase $\varphi_{\mathrm{CC}}(R)$ of the magnetic oscillations at GAM frequency and

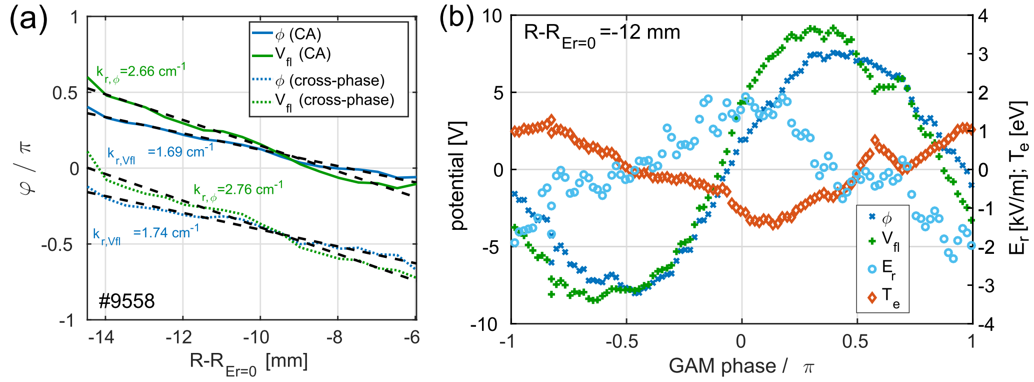

Figure 12. (a) Cross-phase $\varphi_{\rm CC}$ of potential and magnetic fluctuations and phase $\varphi_{\rm CA}$ of the conditionally averaged (CA) fluctuations as a function of the radial position of the probe. Black dashed lines show the linear fit of GAM $k_{\rm r}$. (b) Evolution of the potential, electric field and temperature perturbation at a fixed probe position during an average GAM phase.

a potential measured during the movement of the horizontal probe head. The radial GAM wavenumber $k_{\rm r}$ was then determined by a linear regression as $k_{\rm r} = -\varphi_{\rm CC}(R)/\partial R$.

Second, an instantaneous phase $\varphi_{\rm GAM}$ of the $n = 0$ magnetic oscillations in $\partial B_{\rm r}/\partial t$ from the coil S17 band-passed around GAM peak was determined using Hilbert transform. Since the magnetic signal is measured at a fixed point, independent on the probe position, and the mode frequency is not radially dependent, the phase $\varphi_{\rm GAM}$ can be interpreted as a GAM phase at some fixed, even though unknown radius. This allows to use $\varphi_{\rm GAM}$ as a trigger to compute a conditionally averaged GAM oscillation of the plasma and floating potentials with respect to $\varphi_{\rm GAM}$. The averaging was performed independently for each probe radius and, as it exhibits a harmonic behavior (see figure 12(b)), it was fitted by a harmonic function $V(R,t) = \delta V \cdot \sin(2\pi f_{\rm GAM} t + \varphi_{\rm CA}(R))$. The radial GAM wavenumber $k_{\rm r}$ was then determined similarly as in the first case as $k_{\rm r} = -\varphi_{\rm CA}(R)/\partial R$.

Comparison of $k_{\rm r}$, $\varphi_{\rm CA}(R)$ and $\varphi_{\rm CC}(R)$ of plasma and floating potentials is plotted in figure 12(a). Clearly, both methods well agree and show that GAM potential oscillations at different radii are out of phase, hence, the plasma potential oscillations are accompanied also by oscillations of the radial electric field $E_{\rm r} = -\partial\phi/\partial r$. The radial wavenumber $k_{\rm R}$ of the mode in plasma potential is for the first method $k_{{\rm R},\phi} = 1.74 \pm 0.16\,{\rm cm}^{-1}$ and somewhat larger value is found for $V_{\rm fl}$, $k_{{\rm R},V_{\rm fl}} = 2.76 \pm 0.24\,{\rm cm}^{-1}$, indicating an influence of the temperature field that itself shows even larger wave number $k_{{\rm R},T_{\rm e}} = 5.68 \pm 0.59\,{\rm cm}^{-1}$. Larmor radius in the measured region is $\rho_{{\rm i},T_{\rm i}=T_{\rm e}} \approx 2\,{\rm mm}$ and the GAM radial wavelength $\lambda_{\rm r} = 2\pi/k_{\rm r}$ thus fulfills $\lambda_{\rm r} \gg \rho_{\rm i}$.

Figure 13 shows a 2D space-time plot of the conditionally averaged GAM. The amplitude of the GAM potential oscillations is δV ~ 5–10 V and the amplitude of the radial electric field oscillations computed as a radial derivative of the former is $\delta E_{\rm r}$ ~ 1.5–2.5 kV m^{-1}, in agreement with an estimate $\delta E_{\rm r} \approx k_{\rm r}\delta V$ ~ 1.5 kV m^{-1}. With local $B_{\rm T} = 0.87$ T this corresponds to an amplitude of the poloidal $E \times B$ drift fluctuations in the order of ~2–3 km s^{-1}, i.e. ⩾40% of the maximal magnitude of the poloidal edge flows, and is comparable to the local mean poloidal flow $\langle v_{\rm p}\rangle|_{R=0.726\ {\rm m}} = 2.2$ km s^{-1}. An estimate of the shearing rate caused by GAM gives $\omega_{E\times B} = \partial v_{\rm p}/\partial r = -\partial^2\delta\phi/\partial r^2/B \approx k_{\rm r}^2\delta\phi/B \approx 5 \times 10^5{\rm s}^{-1}$.This value is about a factor of 3 smaller than the shearing rate of the mean flow that peaks around $R_{E_{\rm r}=0}$ with $\max(|\omega_{E\times B}|) \approx 1.5 \times 10^6$ s^{-1}.

Figure 13 also shows that the GAM perturbation propagates radially outward with a radial velocity of propagation of the potentials 0.6–0.8 km s^{-1}. This value is comparable to the velocity $v_{\rm r} \approx 0.6$ km s^{-1} found for the floating potential on the TEXTOR tokamak [10]. On COMPASS, the radial velocity, however, differs between the potentials and the temperature, whose radial propagation is slower. This seems to be consistent with the observed difference in the radial wave numbers, taking into account that for a radially propagating wave it holds $v_{\rm r}k_{\rm r} \approx 2\pi f_{\rm GAM}$.

3.5. GAM interaction with the turbulence

One of the key properties of GAM is its three-wave interaction with turbulent oscillations that drive the mode. Such interaction can be detected using bicoherence [47, 48]. The squared (auto-)bicoherence of a signal $x(t)$ with a Fourier spectrum $X(f)$,

$$b_X^2(f_1, f_2) = \frac{|\langle X(f_1)X(f_2)X^*(f_1+f_2)\rangle|^2}{\left\langle |X(f_1)X(f_2)|^2\right\rangle \langle |X(f_1+f_2)|\rangle},$$

where $\langle\cdot\rangle$ represents an averaging over different segments of the signal, is used to identify frequencies that exchange energy by a non-linear interaction. A typical pattern of high values of bicoherence at $b(f, \pm f_{\rm GAM})$, $b(f_{\rm GAM}, f)$ and $b(f, f \pm f_{\rm GAM})$ for a broad range of frequencies f is expected for GAM [8, 14]. To confirm this property for the mode observed on COMPASS, wavelet bicoherence [48] has been computed in figures 14(a) and (b). While a similar picture can be obtained also using the standard Fourier bicoherence, the wavelet bicoherence appears to be more robust when $f_{\rm GAM}$ oscillates in time and the time series is limited by a fast reciprocation of the probe.

The plot confirms the interaction of GAM with other oscillations in a broad range of frequencies. Moreover, in figure 14(c) we plot summed squared bicoherence defined as $b^2(f) = \sum_{f=f_1+f_2} b^2(f_1,f_2)/N(f)$, where $N(f)$ is the

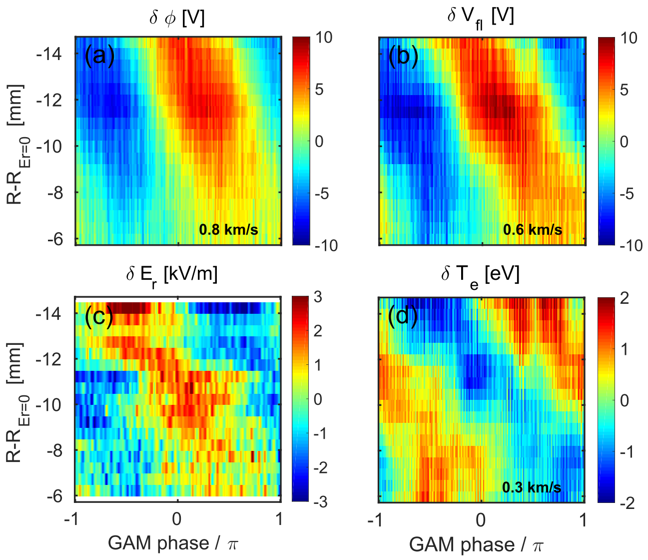

Figure 13. Radial structure and temporal evolution of the conditionally averaged GAM in #9558 in plasma (*a*) and floating (*b*) potentials, radial electric field (*c*) and electron temperature (*d*). The radial velocity of propagation was estimated from a movement of the position of zero perturbation by linear regression.

number of Fourier components in the summation, and compare it with cross-coherence between local plasma potential and $I_{\rm sat}$ measurements. The plot indicates that GAM nonlinearly exchanges energy mainly with fluctuations in the frequency range 100–500 kHz that correspond to coherent structures of the ambient turbulence.

A turbulent drive of GAM may then explain the fact that the GAM is observed in L-mode only, disappearing whenever the turbulence is suppressed during an L-H transition and reappearing shortly after the H-L back transition when the turbulence recovers, as shown in figure 15(*a*) (#8967, $I_{\rm p} = 270$ kA, $n_{\rm e} = 6$–12×10^{19} m^{-3} ramp-up, $q_{95} = 2.5$).

Interestingly, the bicoherence is more pronounced in the floating potential than in the plasma potential, indicating non-negligible contribution also from the temperature field. We note that the difference is not caused by the different measurement techniques (BPP versus LP): when the LP becomes self-emissive and both probes measure a similar potential, the difference in the bicoherence disappears.

4. Change of GAM amplitude with NBI heating

Most of the GAM properties studied in the previous chapters were obtained in ohmic plasmas. Even though a detailed study of the influence of NBI on the GAM properties is beyond the scope of this paper, we still find interesting to demonstrate how the NBI can change GAM.

During the additional on-axis tangential NBI heating, the GAM frequency increases with the increase of plasma temperature. The GAM amplitude changes as well, however, differently for a co-current (CO) and counter-current (CNT) injection (figure 16, $I_{\rm p} = 180$ kA, $n_{\rm e} = 4 \times 10^{19}$ m^{-3}, $q_{95} = 3.7$). While the GAM amplitude is slightly increased during CNT-NBI, the mode is strongly suppressed during CO-NBI. The behavior resembles observations on other machines [12, 21], reporting easier GAM excitation during CNT-NBI heating than during CO-NBI. Nevertheless, on COMPASS the NBI does not generate a new GAM but rather modifies GAM already existing in ohmic plasmas, without presence of fast ions. Below we discuss two ways how the GAM amplitude could be affected by a direction of the NBI heating.

First, the GAM growth rate $\gamma_{\rm GAM}$ could be modified through an interaction with fast resonant particles. In [29] it is shown for the case of a slowed-down velocity distribution of fast ions with strongly peaked pitch angle distribution of the form $f_0 = n_{\rm b}(r)\delta(\chi - \chi_{\rm b})\eta(v_{\rm b} - v)/v^3$ that GAM can be influenced by the fast ions differently for CO- and CNT-NBI. Here $n_{\rm b}$ and $\chi = v_{\parallel}/v$ is the concentration and pitch angle of the fast particles, respectively, δ is a delta function and η is a step function.

The mode growth rate due to the interaction with fast particles is predicted smaller for CO-NBI than CNT-NBI, which may explain differences in the generation of a new EGAM by NBI observed elsewhere. Moreover, there is a region of parameters where the growth rate is negative and presence of the fast particles could lead to a stabilization of an existing mode. The stabilization can appear due to spatial inhomogeneity of the fast particles, which acts for any χ to stabilize/destabilize the mode in the case of CO/CNT injection, assuming $\partial n_{\rm b}/\partial r < 0$, or due to velocity anisotropy of the fast particles that stabilizes the mode for $\chi^2 > 0.6$ and destabilizes otherwise, independently on the beam direction. Due to the effect of the spatial inhomogeneity the stabilization is more likely to happen in the CO-NBI case, but the growth rate can be negative even for CNT-NBI if the effect of the velocity anisotropy overcomes the effect of the spatial inhomogeneity.

To estimate the region of pitch angles that could cause GAM damping on COMPASS, a boundary between regions of the positive and negative growth rates was plotted for the CO-NBI case in figure 17(*a*). In the CNT-NBI case the growth rate was positive everywhere except the largest pitch angles in the central plasma ($|\chi| > 0.9$, $\Psi_{\rm N} < 0.25$). The growth rates were evaluated based on the experimental profiles shown in figure 17(*b*) using relation for GAM frequency and growth rate (59) in [29] that is valid in low-beta plasmas. Only the branch that corresponds in the limit $n_{\rm b} = 0$ to the standard GAM frequency is considered. Comparison of the most common pitch angle estimated with FAFNER code for COMPASS cases modelled in [49] with the minimum pitch angle needed for GAM damping in figure 17(*a*) indicates that during CO-NBI the fast particles can be present in the region where they can decrease the GAM amplitude. Nevertheless, this optimistic estimate does not take into account that the full distribution function will be significantly broader in χ than the assumed δ-function, as the energy of fast particles quickly, on a millisecond time scale, slides down towards the critical energy $E_{\rm c} = 14.8T_{\rm e}[(A_{\rm NBI}^{3/2}/n_{\rm e})\sum_i n_i Z_i^2/A_i]^{2/3}$, where the pitch-angle scattering becomes important due to ion–ion collisions [50]. Here $A_{\rm NBI}$ is the mass number of NBI ions and A_i and Z_i are the mass and charge numbers of the plasma ion species.

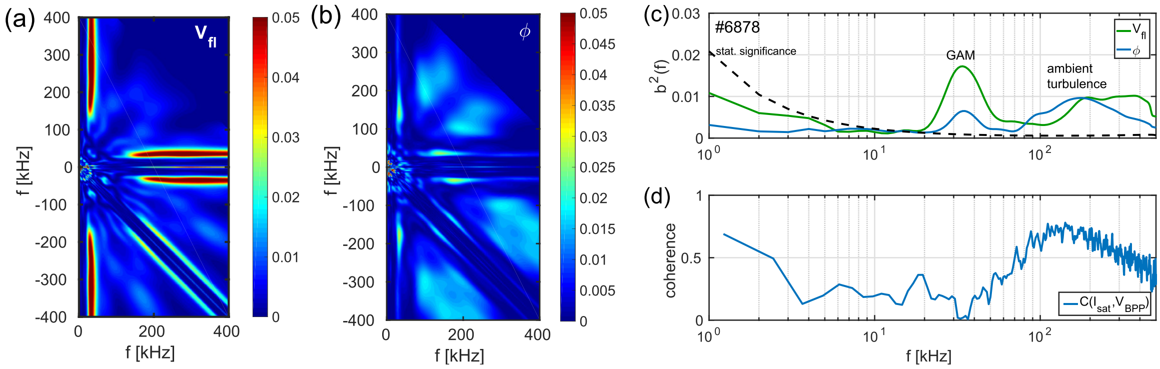

Figure 14. Wavelet bicoherence of floating (a) and plasma (b) potential in #6878. Summed squared bicoherence is shown in (c) and cross-coherence of I_{sat} and ϕ in (d).

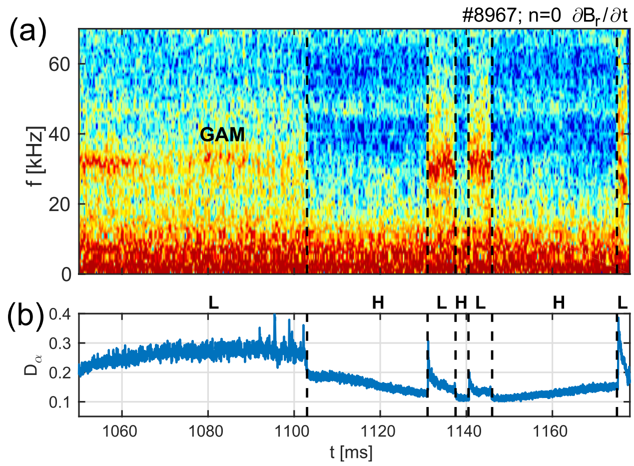

Figure 15. Spectrogram of $\partial B_{\mathrm{r}}/\partial t$ in the divertor region (a) showing GAM behavior during L-H and H-L transitions detected from D_α signal (b).

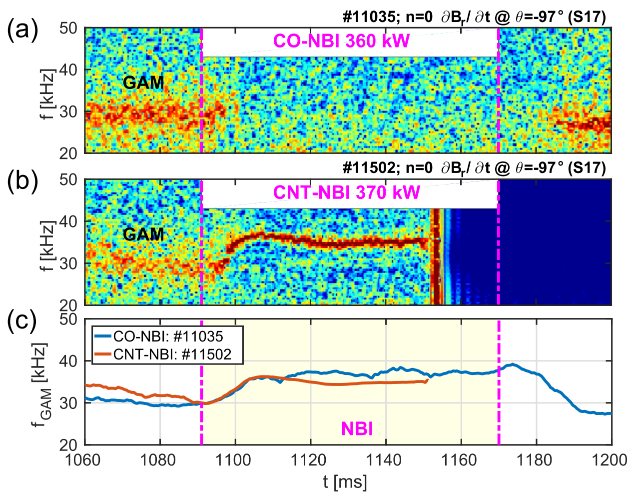

Figure 16. Spectrogram of the $n = 0$ $\partial Br/\partial t$ fluctuations in the divertor region showing frequency and amplitude of GAM magnetic component during CO-NBI (a) and CNT-NBI (b) heating. GAM frequency estimated by Hilbert transform is compared in (c). The CNT-NBI discharge ended with disruption at 1153 ms.

Therefore, we also consider second theory developed in [51, 52] that uses kinetic treatment to study the effect of the electron current combined with the ion flow, modelled by a

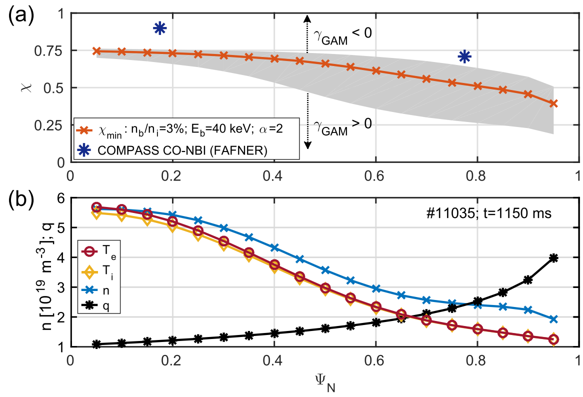

Figure 17. Minimum pitch angle $\chi_{\min}$ of fast ions needed for $\gamma_{\mathrm{GAM}} < 0$ (a), computed for CO-NBI discharge #11035 with parameters shown in (b). The orange line in (a) shows $\chi_{\min}$ for one particular set of parameters with beam energy $E_{\mathrm{b}} = m_{\mathrm{i}}v_{\mathrm{b}}^2/2$ equal to $E_{\mathrm{NBI}} = 40\,\mathrm{keV}$. The gray area shows the region in which $\chi_{\min}$ lies when the parameters are varied in the range $E_{\mathrm{b}} = 20$–$40\,\mathrm{keV}$, $n_{\mathrm{b}}/n_{\mathrm{i}} = 1$–$5\%$ and $n_{\mathrm{b}} \propto (1 - r^2/a^2)^\alpha$ with $\alpha = 1$–4. The blue stars show an estimate of the most common particle pitch angle based on the FAFNER model.

shifted Maxwell distribution with mean velocity $v_{\mathrm{i/e0}}$, on the GAM instability. The GAM instability is predicted to occur when $v_{\mathrm{e0}} > Rq\omega_{\mathrm{GAM}}$. When v_{e0} is in the studied cases estimated from the EFIT current profile, the condition is fulfilled in the central plasma, but not at the edge ($\Psi_{\mathrm{N}} > 0.75$), where the safety factor q increases.

The condition for the GAM instability to appear when the electron current velocity combined with the ion flow overcomes Landau damping is more precisely given by [51]:

$$\gamma_{\mathrm{GAM}} \propto \frac{v_{\mathrm{e0}}}{v_{T_{\mathrm{e}}}}\left[\frac{\rho_L}{4L_n h_\theta}\left(2+2\eta_{\mathrm{i}}+3\frac{T_{\mathrm{e}}}{T_{\mathrm{i}}}\right)+\frac{v_{\mathrm{i0}}}{v_{T_{\mathrm{i}}}}-0.03\frac{v_{T_{\mathrm{e}}}}{v_{\mathrm{e0}}}\exp\left(2-\frac{q^2}{2}\right)\right]\geqslant 0, \quad (6)$$

where $L_n = -n/(\partial n/\partial r)$, $\eta_{\mathrm{i}} = \partial \ln T_{\mathrm{i}}/\partial \ln n$ and $h_\theta = B_\theta/B_0$. The GAM growth rate γ_{GAM} involves a cross-term of the electron and ion velocities $v_{\mathrm{i0}}v_{\mathrm{e0}}$, which may be modified during the beam injection. After the ion energy slides down to the critical energy, beam momentum is transferred to the bulk plasma by ion–ion collisions, shifting v_{i0} in the opposite directions for CNT- and CO-NBI. As a result, the change of v_{i0} increases the GAM growth rate for the former and decreases for the latter and if large enough, it could result in a reduction of the

GAM amplitude [52]. Estimating the momentum transfer as $|\Delta v_{i0}| \approx n_b/n_i v_c$ where we used $n_b/n_i \approx 3\%$ and v_c is the critical beam velocity corresponding to the critical energy at which the transfer of energy to bulk ions becomes important, the velocity change in COMPASS conditions $|\Delta v_{i0}| \approx 0.2 v_{T_i}$ is comparable to the first term in (6) and in the edge, where $\exp(2 - q^2/2)$ drops, also to the last term. This shows that Δv_{i0} can be large enough to significantly affect GAM growth rate in the condition (6).

The first estimates indicate that both mechanisms could influence GAM amplitude during directed NBI heating, each in a different regime of the pitch angle distribution. To draw a definite conclusion and to quantify their individual role in the observed GAM suppression, a dedicated modelling of a velocity distribution of the fast ions together with a better knowledge of the radial mode localization will be needed.

5. Discussion and summary

Geodesic acoustic mode has been identified in COMPASS plasmas based on its distinctive properties, namely frequency scaling with ion sound speed, spatial structure of the mode and its non-linear interaction with a broad-band turbulence. While the mode has been detected in diverted as well as limited plasmas, its properties were analyzed mostly in the diverted configuration where the mode is more accessible by the available diagnostics due to its localization closer to the edge of the plasma and due to its strong magnetic component.

The difference in the position of the GAM edge correlates with the position where the collisional GAM damping starts to sharply increase due to a steep decrease of the temperature profile towards SOL, which is found more inwards in limited plasmas with low elongation.

The GAM frequency was shown to vary with the plasma heating by the neutral beam injection, proportionally to the change of ion sound speed at the plasma edge. Moreover, the frequency was found to periodically oscillate with the period of the sawtooth instability, suggesting modulation of the frequency by a periodic increase of the edge temperature due to expulsion of energy from the plasma core. In the radial direction the frequency does not change with a temperature profile, indicating non-local nature of the GAM mode. This observation was, however, limited by the radial range accessible by the reciprocating probes, and thus it currently cannot by concluded how deep into the plasma does the mode continue and its full radial extent is a subject of further research.

We note that evaluation of the Alfvén-sound continuum based on experimental profiles was carried out for the diverted cases with a linear MHD code KINX [53]. The results do not show presence of gaps in the continuum and thus, according to this computation, only a local continuum GAM should exist at the plasma periphery. Since a non-local GAM was observed experimentally, some other mechanism must be responsible for its formation.

In diverted plasmas the GAM was found to exhibit magnetic oscillations in a narrow band of frequencies created by a single dominant mode, both in the poloidal and radial components of the field. In limited plasmas, the magnetic oscillations are much weaker, for small q_{95} often below the level of background, and broadband (25–100 kHz), suggesting presence of a continuum GAM. The relative amplitude of the broadband oscillations was found to scale with q_{95}, as one would expect if governed by Landau damping, which explains why the GAM magnetic component was not previously detected on COMPASS in low-q low-κ_b plasmas.

Investigation of GAM poloidal structure revealed long range correlations of the plasma potential between different points on a single flux surface, consistent with the mode numbers $m_\phi/n \approx 0/0$. Magnetic oscillations were shown to have a form of an axisymmetric poloidal standing wave. Its poloidal structure is somewhat deformed compared to the $m_B = 2$ prediction for an ideal circular plasma and the mode exhibits regions with an altered phase of oscillations. Their amplitude is, however, small compared to the main structure. Poloidal structure of the continuum GAM differs from the diverted one mainly in the divertor region, due to a presence/absence of the X-point. With X-point, the amplitude is strongest at the poloidal angle corresponding to a position of the outer strike-point where the oscillations are not present at all in the limited plasmas. The oscillations of the continuum GAM are visible only around $\theta \approx \pm(90\text{–}135)^\circ$, consistent with $m_B = 2$ structure, nevertheless detected only on HFS.

The bicoherence analysis confirmed that the mode non-linearly exchanges energy with the ambient turbulence. Significant difference was found in the auto-bicoherence of the floating and plasma potential. This indicates non-negligible contribution of the temperature field in the bicoherence of $V_{\rm fl}$, which may lead to an overestimation of the energy exchange between GAM and the local turbulence when a common assumption $V_{\rm fl} \approx \phi$ is used due to non-availability of a direct ϕ measurement.

Interestingly, different values of the GAM radial wavelength were found for the plasma potential and for the temperature, $\lambda_\phi \sim 4$ cm and $\lambda_{T_e} \sim 1$ cm, respectively, accompanied also by different velocities of radial propagation of both fields, such that $v_r/\lambda \approx$ const. Amplitude of the plasma potential oscillations ~5–10 V results in an oscillating radial electric field with an amplitude in the order of several kV m^{-1}. The associated oscillating $E \times B$ drift can reach the amplitude of the local mean flow. The shearing rate of GAM was estimated as 5×10^5 s^{-1}, by a factor of 3 smaller than the maximal shearing rate of the mean flow. Taking into account that the GAM effective shearing rate will be further reduced due to the large frequency of the oscillations [3], the impact of the mode on turbulence is expected to be rather low compared to the mean flow or to low-frequency zonal flows.

In the last section we reported a significant reduction of the GAM magnetic signal during co-current but not counter-current NBI heating. In contrast to the observations on other machines [12, 21] where NBI destabilizes a new energetic particle driven mode, NBI on COMPASS modifies the amplitude of a mode already existing in ohmic plasmas, i.e. not driven by energetic particles. Two mechanisms how the directed NBI could influence GAM amplitude were proposed. First, if the instability due to a combined effect of the electron current and ion flux [51, 52] contributes to the GAM growth rate, the NBI driven change of the bulk ion velocity by fast particles around or below the critical energy may increase or decrease GAM growth rate for counter- or co-current injection, respectively, i.e. in the same manner as observed in the experiment. Nevertheless, our estimates show that the condition for the electron driven instability itself is not fulfilled in the edge where GAM is observed. Second, solution of a GAM continuum equation from [29] showed that in the CO-NBI case the GAM growth rate in the edge could be decreased by an interaction with fast resonant particles with high pitch angles. Quantitative impact of both mechanisms on the growth rate and frequency of the edge GAM remains a subject of a further research. Modelling of the fast ions distribution together with an improved experimental characterization of the radial mode localization is being prepared.

Acknowledgment

Authors are grateful to Dr. S. Yu. Medvedev for the computations of the Alfven continuum with KINX code, Dr. J. Urban for providing the results of the FAFNER code and Dr. A. G. Elfimov for a discussion of the NBI effects. This work was supported by grants of the Czech Science Foundation GA16-25074S, GA14-35260S (Thomson scattering measurement), GA16-24724S (NBI modelling), GA15-10723S (electronics of the horizontal probe) and co-funded by MEYS projects number 8D15001 and LM2015045. This work has been carried out within the framework of the EUROfusion Consortium and has received funding from the Euratom research and training programme 2014–2018 under grant agreement No 633053. The views and opinions expressed herein do not necessarily reflect those of the European Commission. Access to computing and storage facilities owned by parties and projects contributing to the National Grid Infrastructure MetaCentrum provided under the programme 'Projects of Large Research, Development, and Innovations Infrastructures' (CESNET LM2015042), is appreciated. Research and data analysis done by Kurchatov team for chapter 3 were funded by Russian Science Foundation, Project 14-22-00193. The work of AVM was partly supported by the Competitiveness Programme of NRNU MEPhI.

ORCID iDs

J. Krbec https://orcid.org/0000-0002-3780-6257
J. Horacek https://orcid.org/0000-0002-4276-3124

References

[1] Winsor N. *et al* 1968 *Phys. Fluids* **11** 2448
[2] Diamond P.H. *et al* 2005 *Plasma Phys. Control. Fusion* **47** R35
[3] Hahm T.S. *et al* 1999 *Phys. Plasmas* **6** 922
[4] Tynan G.R. *et al* 2016 *Plasma Phys. Control. Fusion* **58** 044003
[5] Askinazi L.G. *et al* 2017 *Plasma Phys. Control. Fusion* **59** 014037
[6] Cziegler I. *et al* 2013 *Phys. Plasmas* **20** 055904
[7] Wang G. *et al* 2013 *Phys. Plasmas* **20** 092501
[8] Ido T. *et al* 2006 *Plasma Phys. Control. Fusion* **48** S41
[9] Melnikov A.V. *et al* 2015 *J. Phys.: Conf. Ser.* **591** 012003
[10] Xu Y. *et al* 2011 *Plasma Phys. Control. Fusion* **53** 095015
[11] Berk H. *et al* 2006 *Nucl. Fusion* **46** S888
[12] Nazikian R. *et al* 2008 *Phys. Rev. Lett.* **101** 185001
[13] Fu G.Y. 2008 *Phys. Rev. Lett.* **101** 185002
[14] Nagashima Y. *et al* 2005 *Phys. Rev. Lett.* **95** 095002
[15] Melnikov A.V. *et al* 2017 *Nucl. Fusion* **57** 072004
[16] Wahlberg C. *et al* 2016 *Plasma Phys. Control. Fusion* **58** 075014
[17] Smolyakov A.I. *et al* 2010 *Nucl. Fusion* **50** 054002
[18] Bashir M.F. *et al* 2014 *Phys. Plasmas* **21** 082507
[19] Wahlberg C. 2009 *Plasma Phys. Control. Fusion* **51** 085006
[20] de Meijere C.A. *et al* 2014 *Plasma Phys. Control. Fusion* **56** 072001
[21] Matsunaga G. *2012 Proc. 39th EPS Conf. on Plasma Physics (Stockholm, Sweden, 2–6 July 2012) Europhysics Conf. Abstracts* vol 36F P2.062 (http://ocs.ciemat.es/epsicpp2012pap/pdf/P2.062.pdf)
[22] Melnikov A.V. *et al* 2006 *Plasma Phys. Control. Fusion* **48** S87
[23] Conway G. *et al* 2008 *Plasma Phys. Control. Fusion* **50** 055009
[24] Simon P. 2016 *Plasma Phys. Control. Fusion* **58** 045029
[25] Angelino P. *et al* 2008 *Phys. Plasmas* **15** 062306
[26] Gao Z. 2011 *Plasma Sci. Technol.* **13** 15
[27] Leering S. *et al* 2012 *Phys. Rev. Lett.* **109** 165001
[28] Melnikov A.V. *et al* 2015 *Nucl. Fusion* **55** 063001
[29] Kolesnichenko Y.I. *et al* 2013 *Plasma Phys. Control. Fusion* **55** 125007
[30] Gao Z. *et al* 2008 *Phys. Plasmas* **15** 072511
[31] Panek R. *et al* 2016 *Plasma Phys. Control. Fusion* **58** 014015
[32] Adámek J. *et al* 2010 *Contrib. Plasma Phys.* **50** 854
[33] Adámek J. *et al* 2016 *Rev. Sci. Instrum.* **87** 043510
[34] Adámek J. *et al* 2014 *Contrib. Plasma Phys.* **54** 279
[35] Schrittwieser R. *et al* 2002 *Plasma Phys. Control. Fusion* **44** 567
[36] Garcia O.E. *et al* 2007 *Plasma Phys. Control. Fusion* **49** B47
[37] Muller H.W. *et al* 2011 *Nucl. Fusion* **51** 073023
[38] Hidalgo C. *et al* 1991 *Nucl. Fusion* **31** 1471
[39] Markovic T. *et al* 2016 *Nucl. Fusion* **56** 092010
[40] Aftanas M. *et al* 2012 *Rev. Sci. Instrum.* **83** 10E350
[41] Bohm P. *et al* 2014 *Rev. Sci. Instrum.* **85** 11E431
[42] Zajac J. *et al* 2012 *Rev. Sci. Instrum.* **83** 10E327
[43] Gao Z. 2013 *Phys. Plasmas* **20** 032501
[44] Kramer-Flecken A. *et al* 2009 *Plasma Phys. Control. Fusion* **51** 015001
[45] Markovsky I. *et al* 2007 *Signal Process.* **87** 2283
[46] Beall J.M. *et al* 1982 *J. Appl. Phys.* **53** 3933
[47] Kim Y.C. *et al* 1979 *IEEE Trans. Plasma Sci.* **PS-7** 120
[48] van Milligen B.P. *et al* 1995 *Phys. Plasmas* **2** 3017
[49] Urban J. 2010 *Plasma Phys. Control. Fusion* **52** 045008
[50] Speth E. 1989 *Rep. Prog. Phys.* **52** 57
[51] Elfimov A.G. *et al* 2015 *Phys. Plasmas* **22** 114503
[52] Elfimov A.G. *et al* 2017 *Phys. Lett.* A **381** 3066–70
[53] Degtyarev L.M. *et al* 1997 *Comput. Phys. Commun.* **103** 10